Invited Paper

Imaging of Diffusing Media by a Progressive Iterative Backprojection Method Using Time-Domain Data

R. L. Barbour†, H. L. Graber, and J. Lubowsky
Departments of Pathology and Biophysics, SUNY Health Science Center at Brooklyn, 450 Clarkson Ave., Brooklyn, NY 11203

R. Aronson
Department of Physics, Polytechnic University, 333 Jay St. Brooklyn, NY 11201

B. B. Das, K. M. Yoo, and R. R. Alfano
Institute for Ultrafast Spectroscopy and Lasers, Departments of Electrical Engineering and Physics, City College of the City University of New York, NY, NY 10031

†Author to whom inquiries should be addressed.

Abstract

A method for the reconstruction of 3-D images of the interior of dense scattering media, based on the analysis of time-resolved backscattered signals is described. The method evaluates a linear perturbation equation by a progressive iterative backprojection scheme. A key feature of the method is the use of weighting functions which estimate the impact that absorption of photons in the interior have on the response of detectors located at the surface. Examples of reconstructed images shown are based on the analysis of simulated data for multilayered media and simulated and experimental data for media containing finite-volume absorbers. These results contain features which indicate that images having high resolution are obtainable even in the limiting case where the view angle is restricted to only backscattered signals and the absorption contrast across an interior boundary is 1%. A general scheme, similar to a layer-stripping approach, is described for the case where signals emerging about a target are measured.

1.0 Introduction

A common theme among almost all imaging technologies used to examine tissue, including X-ray CT, PET, SPECT, acoustic tomography, and others, is their reliance on the detection of coherent (i.e., straight line paths) or nearly coherent signals. This observation is not a coincidence; in many cases the dominant signal is coherent, and because the paths of the detected radiation are well-defined, this acts to greatly simplify the computational effort required for image reconstruction. Even MRI can be considered a coherent imaging method, as the volume of target medium contributing to the detector response is well-defined.

While many useful applications based on this scheme have been identified, for many types of media the ability to detect coherent signals represents a special case. That is, the fact that such signals exist at all means that the penetrating radiation interacts only weakly with the target medium. In addition, even under these conditions, if the thickness of the target medium is large relative to the scattering pathlength, then at large depths in the medium the intensity of the coherent component becomes vanishingly small while that of the diffusely scattered signal can become dominant. Moreover, there are many instances where the incident radiation interacts strongly with the target medium and is intensely scattered (e.g., tissue at optical frequencies). Here the measurable penetration depth of coherent radiation is very small. Thus, in a general sense, the ability to detect coherent signals becomes a matter of scale.

For many practical applications, imaging schemes based on the analysis of diffusely scattered radiation would permit use of a much broader frequency range of penetrating radiation, while also potentially allowing for imaging to much greater depths than currently is achievable. Further, although scattering significantly complicates the imaging problem, it affords the capacity for remote sensing (i.e., detection of backscattered signals). Thus, diffusion-based imaging schemes could potentially have a much broader application range than current imaging methods.

The practical development of diffusion-based imaging schemes will not be easy. Models of the forward problem are

0-8194-0787-9/92/$4.00

Because the Monte Carlo simulations that calculated the collision densities accumulated them in bins of finite width (i.e., finite time intervals), it was necessary to approximate the integral in equation 3 by a sum. In doing so, it was assumed that the weight could not be accurately calculated to at time resolution better than twice as coarse as that in the collision density data. The discretized version of equation 3 that was used to calculate the weights used in the image reconstructions is:

$$w_{ijk}(N) = \frac{1}{2}\sum_{t_1=1}^{2N} F_{ij}(t_1)\left\{\left[\sum_{t_2=1}^{M-1} F_{ik}(2N-M+1-t_1+t_2)\right] + \frac{1}{2}[F_{ik}(2N+1-t_1) + F_{ik}(2N-M+1-t_1)]\right\} \quad (4)$$

where N = time window index and M = number of collision density bins in weight function time window. If continuous functions for $F_{ij}(t)$ and $F_{ik}(t)$ were available, equation 4 would be equivalent to using the trapezoidal rule to approximate the double integral in equation 3.

2.4 Image reconstruction

The image reconstruction algorithms were based on a perturbation model in which the structure of the test medium is assumed to be close to that of a known reference medium. In that case, the reconstruction reduces to a problem of solving a system of linear equations[3-5]. The successive stages of development of this system are:

$$(I - I_0)_{ijk} = w_{ijk}(\Sigma_a - \Sigma_a^0)_i \quad (5a)$$

$$(I - I_0)_{jk} = \sum_i w_{ijk}(\Sigma_a - \Sigma_a^0)_i \quad (5b)$$

$$\Delta \mathbf{I} = \mathbf{W}\Delta\boldsymbol{\Sigma}_\mathbf{a} \quad (5c)$$

Equation 5a shows that the change in photon flux at the surface for source j and detector k, due to an absorption difference in voxel i, is the product of $\Delta\Sigma_a$ and the weight for that voxel, source, and detector. In equation 5b, we use the approximation that these effects are simply additive, with the net difference ΔI_{jk} equal to the sum of the changes due to $\Delta\Sigma_a$ in all the voxels. Each source-detector pair contributes an equation of the form of 5b to the system in 5c. Equation 5c is fully determined if the number of photon flux measurements is equal to the number of voxels in the medium.

For reasons discussed by Barbour et al.[4] and Wang et al.[17], iterative numerical methods for solving equation 5c are preferable to direct methods. The varieties of reconstruction algorithms used in this study, which are described in the following section, were applicable to both the steady-state and time-resolved situations. The quantities $\Delta\mathbf{I}$ and $\mathbf{W}$ in equation 5c may refer to the detector readings and weights for either type of measurement. In practice, the time-resolved reconstructions yielded faster convergence, and required significantly less time for each iteration, than those employing steady-state data (see Results for quantitative comparison). This is a consequence of the smaller number of calculations performed, which in turn is due to the fact that steady-state weight functions encompass the entire volume involved in the reconstruction, while time-resolved weight functions, at early time intervals, are non-zero in only a small fraction of this volume.

2.5 Variations of the reconstruction algorithm

Several different evaluation schemes have been formulated and tested for the solution of equation 5c. These have included substituting related quantities for $\Delta\mathbf{I}$ and $\mathbf{W}$, as well as varying the order in which the data were evaluated. All of the images presented in this study were obtained using the progressive iterative backprojection algorithm described in Barbour et al[4]. The two parts of each iteration step are:

$$s_i^n = \frac{\sum_j \sum_k w_{ijk}\left[-c_{jk}^{n-1} + \left(\frac{\Delta I}{I_0}\right)_{jk}\right]}{\sum_j \sum_k w_{ijk}} + s_i^{n-1} \quad (6a)$$

$$c_{jk}^{n} = \frac{\sum_i w_{ijk} s_i^n}{\sum_i w_{ijk}} \tag{6b}$$

with $n \geq 1$, and letting $s_i^o = 0$ for all i and $c_{jk}^o = 0$ for all j and k. s_i^n is the n^{th}-iteration estimate of the image density in the i^{th} voxel, c_{jk}^n is the n^{th}-iteration estimate of the relative darkening, $\Delta I/I_o$, for the measurement made with the source j and detector k. Detector readings were evaluated as normalized differences, $\Delta I/I_o$, rather than their absolute differences, ΔI, as the former quantity can more easily account for expected fluctuations in source intensity and detector sensitivity. Answers derived from the two quantities, although different, will be correlated. For steady-state and time resolved measurements, the algorithms employed were progressive in distance or time and distance, respectively. In the latter case, where both time and distance were parameters, the iteration initially incorporated only detector readings corresponding to the smallest source-detector separation r, and earliest time window. Data from the same set of detectors at later times and the next larger r were subsequently included.

For the reconstructions of two- and three-layer media, the assumed knowledge was that the medium was heterogeneous in only the depth dimension, so that ΔI_{jk} was a function of only r and detector orientation. After each application of equation 6a the average value of s_i^n was calculated in each layer, and this was taken to be the image density of all voxels at that depth. The absolute values of the weights were employed in these reconstructions.

Reconstructions of the medium used in the experiments were done with the assumptions that the scattering was isotropic, that the scattering medium had the same refractive index as water, and that the absorber was known to be symmetric about the two major axes of the grid on which the source fiber was scanned.

3.0 Results

3.1 Comparison of Weight Functions for Time-Independent and Time-Gated Measurements

We have previously shown that by evaluating a linear perturbation equation (equation 5c) for backscattered signals, images of subsurface structures can be obtained[3-5]. A key aspect in this approach is the use of estimates of the site-dependent effect of absorption on detected photon flux for each source-detector pair considered. An example of these gradients, referred to here as weights, for time-independent backscattered measurements is shown in Figure 1. These results were calculated, as described in Methods, by evaluating equation 1 for a medium having finite thickness (10 MFP), isotropic scattering, $\Sigma_a/\Sigma_t = .01$ and detectors located 1 (Panel A) and 5 (Panel B) MFP from the source. For illustration purposes, the value of the function in equation 1 has been displayed as a contour plot (X-Z slice) by ranking voxels in order of descending weight by the indicated percentiles. Thus voxels located within the first 10% contour contain the greatest weight and, correspondingly, occupy the smallest total volume (directly beneath the source and detector).

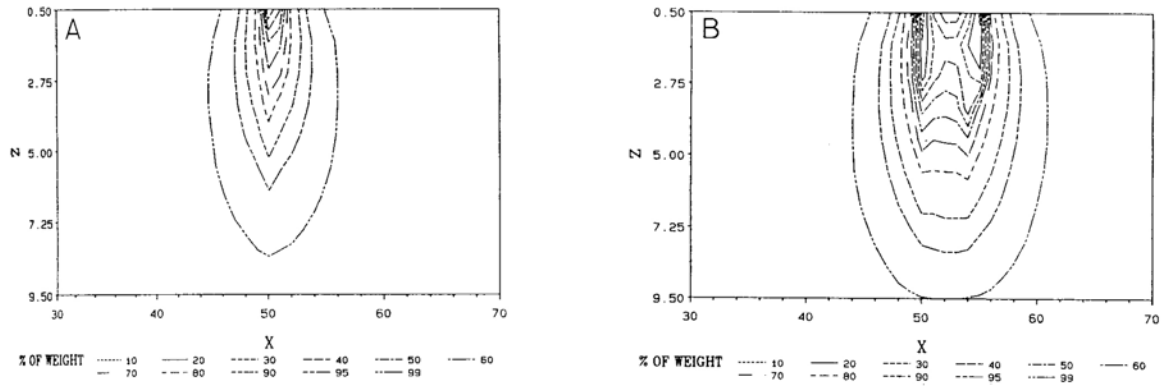

Legend to Figure 1: Contour Plots of vertical sections through steady-state weight functions. Plane of section is y = 50, with light

Because the Monte Carlo simulations that calculated the collision densities accumulated them in bins of finite width (i.e., finite time intervals), it was necessary to approximate the integral in equation 3 by a sum. In doing so, it was assumed that the weight could not be accurately calculated to at time resolution better than twice as coarse as that in the collision density data. The discretized version of equation 3 that was used to calculate the weights used in the image reconstructions is:

$$w_{ijk}(N) = \frac{1}{2}\sum_{t_1=1}^{2N} F_{ij}(t_1)\left\{\left[\sum_{t_2=1}^{M-1} F_{ik}(2N-M+1-t_1+t_2)\right] + \frac{1}{2}[F_{ik}(2N+1-t_1) + F_{ik}(2N-M+1-t_1)]\right\} \quad (4)$$

where N = time window index and M = number of collision density bins in weight function time window. If continuous functions for $F_{ij}(t)$ and $F_{ik}(t)$ were available, equation 4 would be equivalent to using the trapezoidal rule to approximate the double integral in equation 3.

2.4 Image reconstruction

The image reconstruction algorithms were based on a perturbation model in which the structure of the test medium is assumed to be close to that of a known reference medium. In that case, the reconstruction reduces to a problem of solving a system of linear equations[3-5]. The successive stages of development of this system are:

$$(I - I_0)_{ijk} = w_{ijk}(\Sigma_a - \Sigma_a^0)_i \quad (5a)$$

$$(I - I_0)_{jk} = \sum_i w_{ijk}(\Sigma_a - \Sigma_a^0)_i \quad (5b)$$

$$\Delta \mathbf{I} = \mathbf{W}\Delta\boldsymbol{\Sigma}_\mathbf{a} \quad (5c)$$

Equation 5a shows that the change in photon flux at the surface for source j and detector k, due to an absorption difference in voxel i, is the product of $\Delta\Sigma_a$ and the weight for that voxel, source, and detector. In equation 5b, we use the approximation that these effects are simply additive, with the net difference ΔI_{jk} equal to the sum of the changes due to $\Delta\Sigma_a$ in all the voxels. Each source-detector pair contributes an equation of the form of 5b to the system in 5c. Equation 5c is fully determined if the number of photon flux measurements is equal to the number of voxels in the medium.

For reasons discussed by Barbour et al.[4] and Wang et al.[17], iterative numerical methods for solving equation 5c are preferable to direct methods. The varieties of reconstruction algorithms used in this study, which are described in the following section, were applicable to both the steady-state and time-resolved situations. The quantities $\Delta\mathbf{I}$ and $\mathbf{W}$ in equation 5c may refer to the detector readings and weights for either type of measurement. In practice, the time-resolved reconstructions yielded faster convergence, and required significantly less time for each iteration, than those employing steady-state data (see Results for quantitative comparison). This is a consequence of the smaller number of calculations performed, which in turn is due to the fact that steady-state weight functions encompass the entire volume involved in the reconstruction, while time-resolved weight functions, at early time intervals, are non-zero in only a small fraction of this volume.

2.5 Variations of the reconstruction algorithm

Several different evaluation schemes have been formulated and tested for the solution of equation 5c. These have included substituting related quantities for $\Delta\mathbf{I}$ and $\mathbf{W}$, as well as varying the order in which the data were evaluated. All of the images presented in this study were obtained using the progressive iterative backprojection algorithm described in Barbour et al[4]. The two parts of each iteration step are:

$$s_i^n = \frac{\sum_j\sum_k w_{ijk}\left[-c_{jk}^{n-1} + \left(\frac{\Delta I}{I_0}\right)_{jk}\right]}{\sum_j\sum_k w_{ijk}} + s_i^{n-1} \quad (6a)$$

ratio in this region reaches a maximum of approximately 3. At later time intervals, for the same detector location (Panel B, t = 69-70 MFT), the maximum value of the ratio increases to greater than 14 and occurs at greater depths. Thus, for this particular source-detector pair and in the indicated region, a time-gated measurement affords a considerable advantage over a time-independent measurement. The advantage gained by time-gating in a particular region, however, is highly sensitive to which source-detector pair is examined. When a comparison is made for a similar time interval (t = 65-70 MFT) but at a greater source-detector separation (r = 10 MFP, Panel C), the maximum value of this ratio is reduced to only approximately 1.35. In this case it is apparent that, at least for the example shown, little advantage is gained by employing a time-gated measurement.

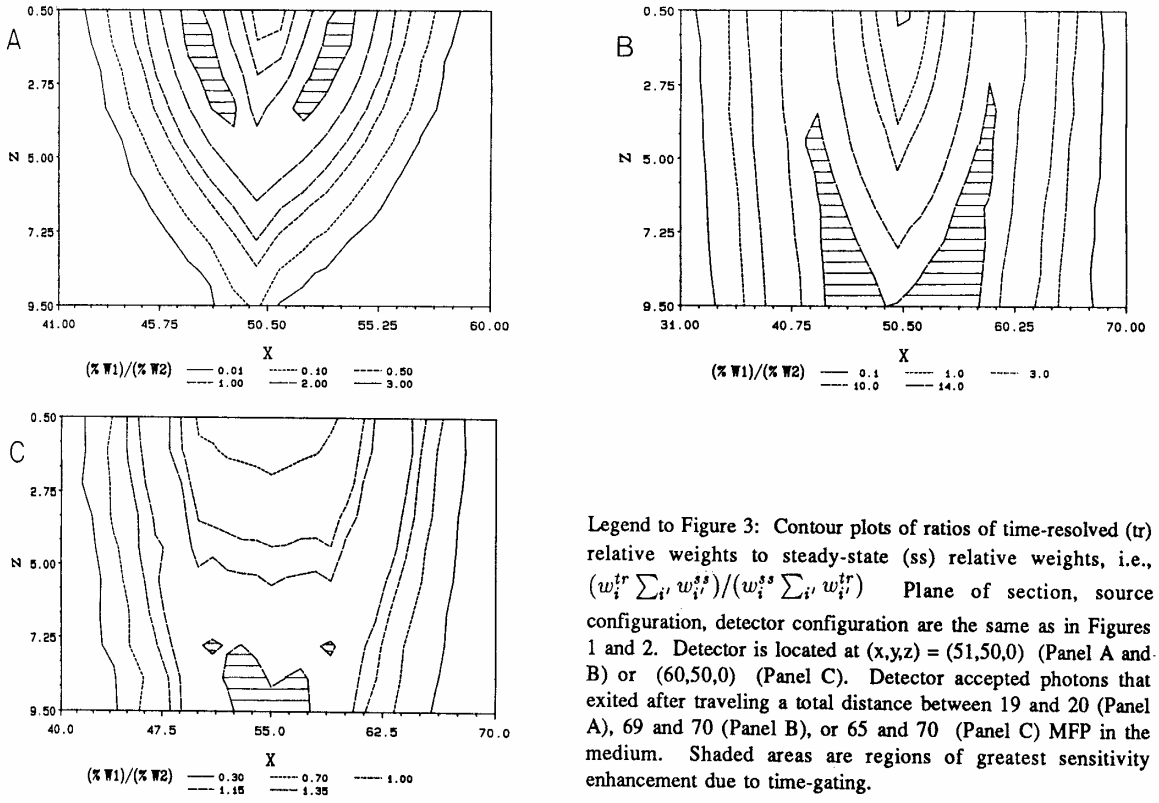

Legend to Figure 3: Contour plots of ratios of time-resolved (tr) relative weights to steady-state (ss) relative weights, i.e., $(w_i^{tr} \sum_{i'} w_{i'}^{ss})/(w_i^{ss} \sum_{i'} w_{i'}^{tr})$ Plane of section, source configuration, detector configuration are the same as in Figures 1 and 2. Detector is located at (x,y,z) = (51,50,0) (Panel A and B) or (60,50,0) (Panel C). Detector accepted photons that exited after traveling a total distance between 19 and 20 (Panel A), 69 and 70 (Panel B), or 65 and 70 (Panel C) MFP in the medium. Shaded areas are regions of greatest sensitivity enhancement due to time-gating.

3.2 Image Reconstruction by Progressive Backprojection for Time-Independent and Time-Gated Signals

Representative plots of reconstructed images obtained by evaluating steady-state and time-resolved data for media containing the "T" shaped absorber are shown in Figures 4 and 5, respectively. A strict comparison is not entirely valid as the number and locations of the source-detector pairs and number of iterations performed are not identical. Steady-state data were evaluated using a scheme progressive in distance (i.e., D_1, D_1D_2, $D_1D_2D_3$, ..., where the family of detectors D_1, D_2, D_3,..., are located at successively greater distances from the source). A similar approach was used to evaluate time-resolved data. An analysis progressive in distance was accomplished by simultaneously considering all time windows for a given family of source-detector pairs (i.e., $D_1(\sum_{t1}^{tn})$, $D_1D_2(\sum_{t1}^{tn})$, $D_1D_2D_3(\sum_{t1}^{tn})$, ..., (Figure 5, panel A and B)). An analysis progressive in time and distance sequentially considered each time window for a particular family of source-detector pairs (i.e., D_{1t1}, D_{1t1t2}, ..., $D_{1t1...tn}$, $D_{1t1...tn}D_{2t1}$, $D_{1t1...tn}D_{2t1t2}$, ..., (Figure 5, Panels C and D)). In order to reduce the computation time and to test the robustness of the algorithm, only a portion of the available data was evaluated. This had the effect of making the problem underdetermined, as the number of observations evaluated were between 18-63% of the number of unknowns. Inspection of Figure 4 shows that whereas the region of greatest darkening coincides reasonably well with the actual location of the absorber, the quality of the image is not good. It should be noted, however, that the detectors whose values were used in the reconstruction were all within 2 transport MFP from a source. At this distance, more than 85% of the total weight lies in

source directed normal to surface at (x,y,z) = (50,50,0). Detector is located at (51,50,0) (Panel A) or (55,50,0) (Panel B), and is inclined 10° from normal, so that axes of source and detector intersect at a point below the surface (z > 0). Weights were calculated by eq. 1 in Methods, and voxels were ranked in order of descending weight. Contours are the intersections of the plane y = 50 with the surfaces bounding the indicated percentiles of the total weight.

One of the difficulties encountered when evaluating steady-state signals is that detected photons have the opportunity to propagate throughout the target medium. At a given detector location, signals from shallow and deep regions are detected simultaneously. Since the latter always have weights much less than voxels located nearer the surface in the vicinity of the source and detector, especially for small source-detector separation distances, it becomes increasingly more difficult to detect the presence of excess absorption in deeper regions. At these depths, the reconstruction problem can become severely underdetermined.

One approach to isolating signals having a given pathlength is to employ time-resolved methods. At early time intervals, the maximum distance the detected photons may have propagated in the medium is sharply limited. Examples of weight functions calculated by using equation 4 for time-gated signals are shown in Figure 2. Results shown are expressed as in Figure 1. At early time intervals (Panel A, t = 9-10 mean free times (MFT) (i.e., time for photons to travel a total distance of 9-10 MFP), r = 5 MFP) all of the detected photons are restricted within a small finite volume. At later times (Panel B, t = 69-70 MFT, r = 5 MFP), this volume has increased greatly, and the volume corresponding to any given contour contains voxels at a greater depth than in the case of time-independent observations (cf., Figure 1, Panel B). In terms of the reconstruction problem, relative to the time-independent case, use of early time signals can greatly reduce the number of voxels which must be scored. Related to this is the observation that, at early times, the uncertainty of paths of detected photons is also less.

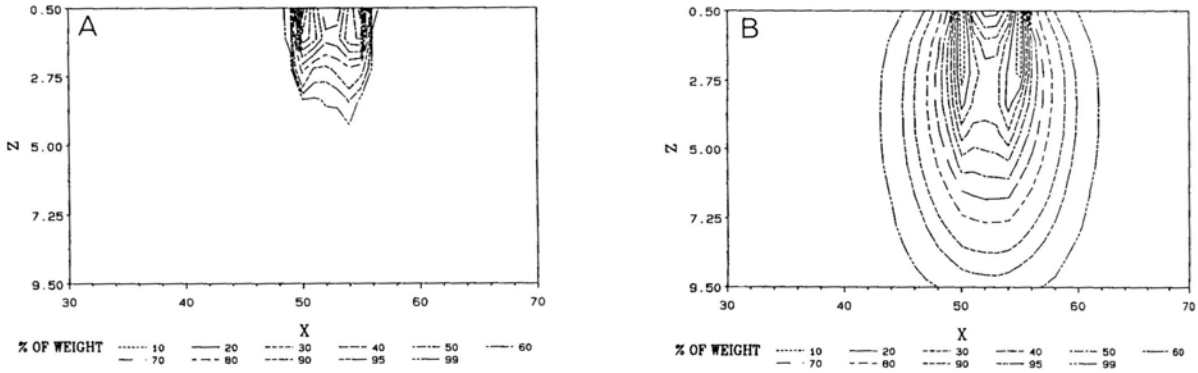

Legend to Figure 2: Contour plots of vertical sections through time-resolved weight functions. Plane of section, source configuration, and detector configuration are the same as in Figure 1B. Detector accepted photons after traveling a total distance between 9 and 10 (Panel A) or between 69 and 70 (Panel B) MFP in the medium. Weights were calculated by eq. 4 in Methods, and presented in the same manner as in Figure 1.

It is of interest to estimate the degree of advantage time-gated measurements should have over time-independent measurements in the reconstruction problem. While this will likely depend on several factors (e.g., selection of source-detector positions, order in which data are evaluated[4], geometry of target medium, spatial location of absorbing regions, type of algorithm employed) a comparison of the value of the weight functions obtained for the same source-detector pair using the different measurement schemes is instructive. Data in Figure 3 shows this comparison for detectors positioned 1 and 10 MFP from the source. Results shown represent a contour plot of the ratio of relative weights (i.e., the fraction of the total weight) in each voxel (time-gated/ time-independent, X-Z slice) at the indicated time intervals. Values of this ratio greater than one indicate a greater sensitivity by time-gated measurements to excess absorption in the medium, while values less than one indicate a greater sensitivity by time-independent measurements. In all three examples a consistent triphasic trend is observed. The value of the ratio of weights for voxels located in the vicinity of the source and detector is less than one. At intermediate distances, the ratio becomes greater than one, followed by a precipitous decline at greater distances. This behavior, although complex, is not unexpected. Interestingly, at early time intervals and for detectors located close to the source (Panel A, r = 1 MFP, t = 19-20 MFT), the position of the region of greater sensitivity for time-gated measurements is located not in between, but outside of, the region between the source and detector, and forms a truncated bowl-shaped structure. In the example shown, the value of the

ratio in this region reaches a maximum of approximately 3. At later time intervals, for the same detector location (Panel B, t = 69-70 MFT), the maximum value of the ratio increases to greater than 14 and occurs at greater depths. Thus, for this particular source-detector pair and in the indicated region, a time-gated measurement affords a considerable advantage over a time-independent measurement. The advantage gained by time-gating in a particular region, however, is highly sensitive to which source-detector pair is examined. When a comparison is made for a similar time interval (t = 65-70 MFT) but at a greater source-detector separation (r = 10 MFP, Panel C), the maximum value of this ratio is reduced to only approximately 1.35. In this case it is apparent that, at least for the example shown, little advantage is gained by employing a time-gated measurement.

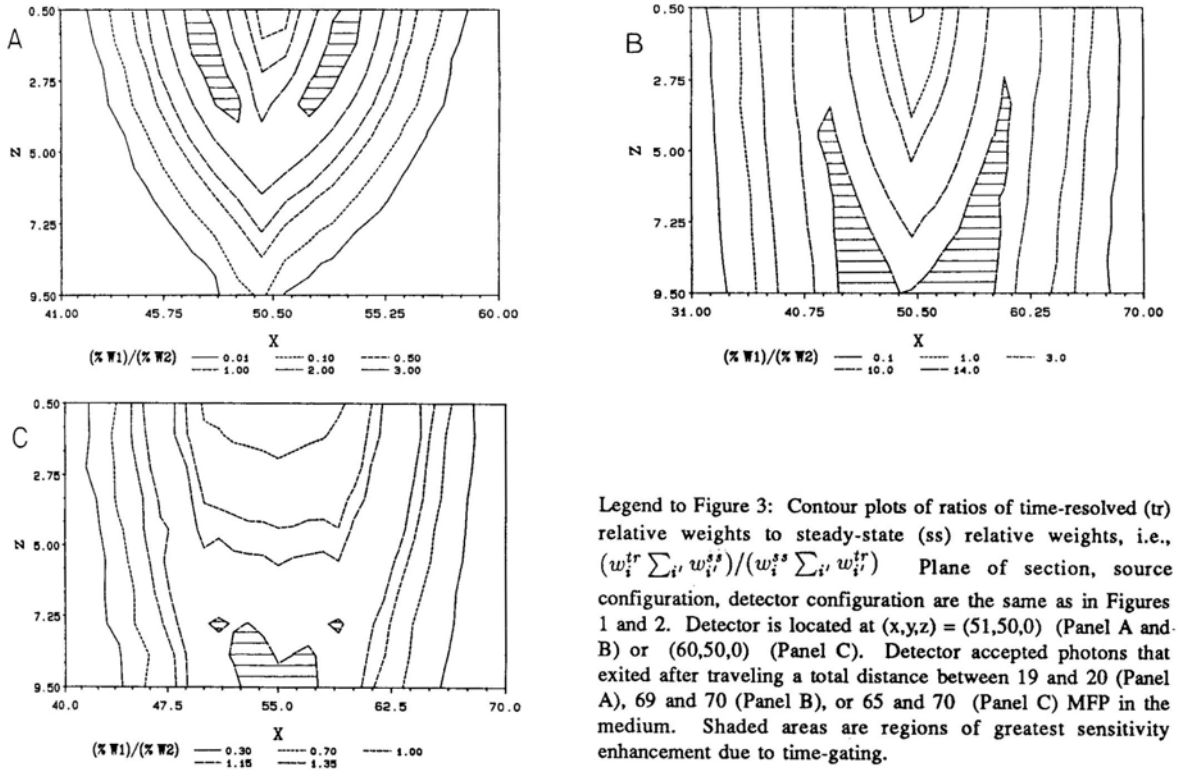

Legend to Figure 3: Contour plots of ratios of time-resolved (tr) relative weights to steady-state (ss) relative weights, i.e., $(w_i^{tr} \sum_{i'} w_{i'}^{ss})/(w_i^{ss} \sum_{i'} w_{i'}^{tr})$ Plane of section, source configuration, detector configuration are the same as in Figures 1 and 2. Detector is located at (x,y,z) = (51,50,0) (Panel A and B) or (60,50,0) (Panel C). Detector accepted photons that exited after traveling a total distance between 19 and 20 (Panel A), 69 and 70 (Panel B), or 65 and 70 (Panel C) MFP in the medium. Shaded areas are regions of greatest sensitivity enhancement due to time-gating.

3.2 Image Reconstruction by Progressive Backprojection for Time-Independent and Time-Gated Signals

Representative plots of reconstructed images obtained by evaluating steady-state and time-resolved data for media containing the "T" shaped absorber are shown in Figures 4 and 5, respectively. A strict comparison is not entirely valid as the number and locations of the source-detector pairs and number of iterations performed are not identical. Steady-state data were evaluated using a scheme progressive in distance (i.e., D_1, D_1D_2, $D_1D_2D_3$, ..., where the family of detectors D_1, D_2, D_3,..., are located at successively greater distances from the source). A similar approach was used to evaluate time-resolved data. An analysis progressive in distance was accomplished by simultaneously considering all time windows for a given family of source-detector pairs (i.e., $D_1(\sum_{t1}^{tn})$, $D_1D_2(\sum_{t1}^{tn})$, $D_1D_2D_3(\sum_{t1}^{tn})$, ..., (Figure 5, panel A and B)). An analysis progressive in time and distance sequentially considered each time window for a particular family of source-detector pairs (i.e., D_{1t1}, D_{1t1t2}, ..., $D_{1t1...tn}$, $D_{1t1...tn}D_{2t1}$, $D_{1t1...tn}D_{2t1t2}$, ..., (Figure 5, Panels C and D)). In order to reduce the computation time and to test the robustness of the algorithm, only a portion of the available data was evaluated. This had the effect of making the problem underdetermined, as the number of observations evaluated were between 18-63% of the number of unknowns. Inspection of Figure 4 shows that whereas the region of greatest darkening coincides reasonably well with the actual location of the absorber, the quality of the image is not good. It should be noted, however, that the detectors whose values were used in the reconstruction were all within 2 transport MFP from a source. At this distance, more than 85% of the total weight lies in

voxels less deep than the absorber. Thus, only a small portion of the incident signal had the opportunity to interact with the target. Despite these limitations, and that the problem was determined to an extent of only 9%, the reconstructed image correctly identifies the existence of asymmetry in the shape of the absorber, and its approximate location.

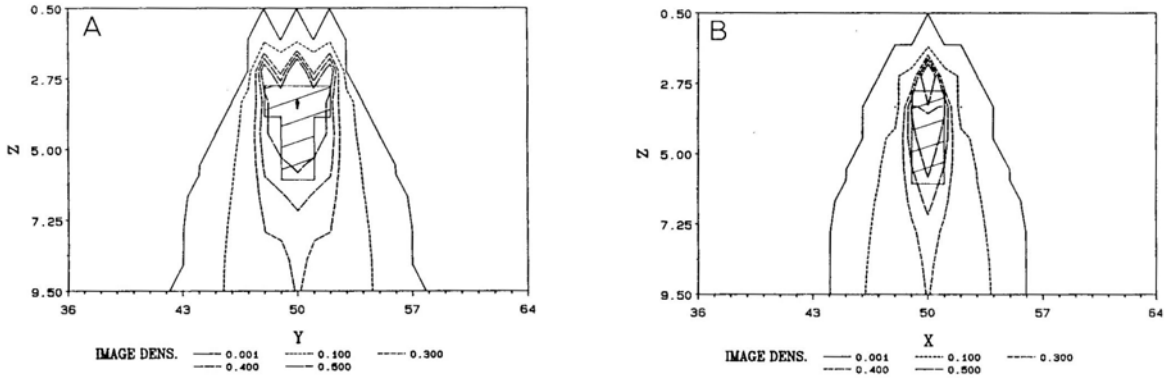

Legend to Figure 4: Contour plots of vertical sections through image of T, reconstructed by equations 6a and 6b, and using steady-state weight functions and reflectance measurements. The planes of section are x = 50 (Panel A) and y = 50 (Panel B), with the true sections through the absorber in these planes shaded in. The medium is infinitely long and wide, 10 MFP thick, scatters photons isotropically, and has $\Sigma_a = .01\Sigma_t$. The absorber is a black body ($\Sigma_a = \infty$) with nonreflective planar boundaries. Reconstruction program employed only readings for detectors at r = 1 in the first 200 iterations, readings for detectors at r = 1 and r = $\sqrt{2}$ in the next 200, and readings for detectors at r = 1, r = $\sqrt{2}$, and r = 2 in the final 200. Readings were obtained at 19 locations of the source beam relative to the absorber, all lying within a circle of radius 6 MFP about the point (50,50,0) on the surface. The symmetry of the absorber effectively increases the number of source positions to 61. Two detector orientations were used at each detector location, one inclined 10^o from the normal, the other inclined 80^o from the normal.

With the above caveats noted, comparison of Figures 4 and 5 reveals that images of much higher resolution can be achieved using time-resolved data. Comparison of Panel A and B to C and D in Figure 5 also indicates that an analysis progressive in time and distance appears to yield an answer having a slightly better edge detection than when the analysis is progressive only in distance, even though the former was less determined (24 vs. 63% respectively) and required approximately 10% less cpu time to evaluate. The maximum depth in the medium to which the image was calculated is less than for the time-independent case, as the longest time window examined (12 MFT) restricted all photons detected to within 6 MFP of the surface. It should also be noted that because of an interpolation routine inherent in the graphics package used to plot the data, the apparent image density gradient observed in the reconstructed images in some cases underestimated the actual gradient. In particular, for Panel D of Figure 5, the horizontal gradient between z = 4 and z = 6 is infinite, indicating that perfect edge detection was achieved.

In the above example, the data used for image reconstruction was based on the presence of a black absorber against a weakly

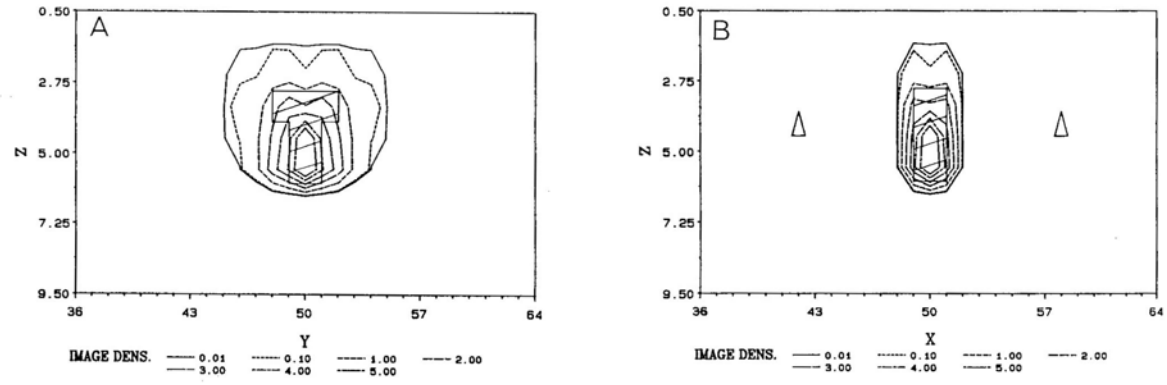

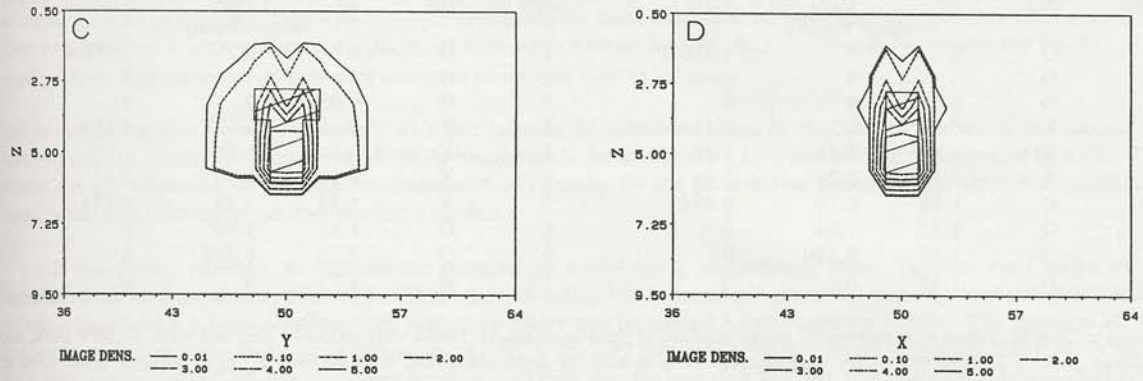

Legend to Figure 5: Contour plots of vertical sections through image of T, reconstructed by equations 6a and 6b, and using time-resolved weight functions and reflectance measurements. Three time windows were employed, corresponding to photons exiting after traveling a total distance in the ranges 0-4, 4-8, and 8-12 MFP in the medium. Progression to the next larger set of detector readings occurred automatically when the rate of decrease of the rms error of the calculated detector readings fell below a preset threshold. Source and detector configurations for the reflectance measurements are the same as in Figure 4, except that only 12 of the 19 source locations were used in this reconstruction (symmetry of absorber increases number to 42). In the reconstruction whose result is shown in Panels A and B, detector readings from all three time windows were brought into the reconstruction at the same time. Program used only readings for detectors at $r = 1$ in the first 117 iterations, readings for detectors at $r = 1$ and $r = \sqrt{2}$ in the next 171, readings for detectors at $r = 1$, $r = \sqrt{2}$, and $r = 2$ in the next 157, and readings for detectors at $r = 1$, $r = \sqrt{2}$, $r = 2$, and $r = \sqrt{5}$ in the final 50. For the reconstruction whose result is shown in Panels C and D, program first used only readings for the smallest value of r and first time window, then added the data from the remaining time windows sequentially, before considering readings obtained at the next larger value of r. The number of iterations performed at each stage were: 2 for $r = 1$, t1; 244 for $r = 1$, t1, t2; 163 for $r = 1$, t1, t2, and t3; 500 for $r = 1$, t1, t2, t3, and $r = \sqrt{2}$, t1; 110 for $r = 1$, t1, t2, t3, and $r = \sqrt{2}$, t1, t2.

absorbing background. For many practical applications, especially for optical measurements of tissue at NIR frequencies, the absorption contrast between different layers of tissue, or the capillary tree and tissue, will be much less. For this reason it was of interest to examine heterogeneous media having low contrast (1-7%). Results shown in Tables 1 and 2 are based on simulations of 3-layer media in which the thickness or absorption, respectively, of the intermediate layer was varied. In all cases a layered structure was assumed, reducing the number of unknowns to 10. A total of 7 time windows was considered, between 0 and 28 MFT in steps of 4 MFT, for a detector located 1 MFP from the source and oriented 10° from vertical. For the first study, the absorption contrast was held constant at 1:5:1% in the top, intermediate and bottom layers respectively; the thickness of the intermediate layer varied from 1-4 MFP, beginning at $z = 4$. Inspection of the Table reveals that in all cases the algorithm correctly identified the presence of an intermediate layer. The observation that no absorption was detected at depths below $z = 7$ indicates that the algorithm was able to "see through" the intermediate layer and correctly determine the lack of excess absorption

Table 1: Three Layer Absorber Problem - Variable Boundary (Σ_a/Σ_t = .01: .05: .01)

		Iteration Number					Iteration Number		
Layer	Orig	20	1000	7200	Layer	Orig	20	1000	7200
		Image Density					Image Density		
1	O	0	0	9.33E-5	1	O	0	0	1.44E-4
2	O	0	0	0	2	O	0	0	0
3	O	0.0389	0	0	3	O	0.0365	0	0
4	X	0.319	0.267	0.201	4	X	0.428	0.262	0.186
5	O	0.587	0.944	1.29	5	X	0.825	1.36	1.70
6	O	0.711	1.10	0.688	6	O	1.04	1.88	1.83
7	O	0.755	0.729	0	7	O	1.14	1.62	0
8	O	0.743	0.0124	0	8	O	1.15	0.767	0
9	O	0.722	0	0	9	O	1.13	0	0
10	O	0.694	0	0	10	O	1.10	0	0

Layer	Orig	20	1000	7200	Layer	Orig	20	1000	7200
		Image Density					Image Density		
1	O	0	0	1.83E-4	1	O	0	0	1.93E-4
2	O	0	0	0	2	O	0	0	0
3	O	0.0331	0	0	3	O	0.0321	0	0
4	X	0.457	0.241	0.164	4	X	0.463	0.233	0.161
5	X	0.898	1.48	1.80	5	X	0.916	1.50	1.80
6	X	1.16	2.21	2.34	6	X	1.19	2.30	2.47
7	O	1.28	2.10	0.076	7	X	1.32	2.29	0.373
8	O	1.31	1.34	0	8	O	1.35	1.60	0
9	O	1.30	0.320	0	9	O	1.35	0.618	0
10	O	1.27	0	0	10	O	1.33	0	0

Legend to Table 1: Values of reconstructed image densities of three-layer media. Media were infinitely long and wide, 10 MFP thick, and scattered photons isotropically. They were heterogeneous in only the depth dimension, with the ratio Σ_a/Σ_t in the three layers fixed at .01:.05:.01, the superficial layer boundary fixed at z = 3, and the thickness or the intermediate layer varied between 1 and 4 MFP. Detector readings from seven time windows were employed, ranging from 0-4 MFT to 24-28 MFT in steps of 4 MFT, and all for detectors at r = 1. Due to the layered structure, there were only ten unknowns in the reconstruction problem.

in the deeper layers. The reconstructed images shown are, however, clearly imperfect. The image density is not uniform, and for media having thinner inclusions edge blurring is evident and the depth of maximum density is incorrect by one layer.

Results of reconstructed images of media in which the contrast of the intermediate layer was varied between 1% and 7% are shown in Table 2. In these studies, the thickness of the intermediate layer was held constant at 4 MFP, beginning at layer 4. Inspection of the Table 2 shows that even in the case where the absorption contrast is only 1% above background, the reconstructed image correctly identified the presence of the intermediate layer. In addition, the lack of excess absorption in the

Table 2: Three Layer Absorber Problem - Variable Contrast (Boundary Z = 4 - 7)

Σ_a/Σ_t(.01: .02: .01) Iteration Number

Layer	Orig	20	1000	5000
		Image Density		
1	O	0	0	1.46E-4
2	O	0	0	1.25E-4
3	O	0.0772	0	2.14E-6
4	X	0.130	0.053	0.0384
5	X	0.264	0.423	0.472
6	X	0.350	0.722	0.794
7	X	0.398	0.827	0.516
8	O	0.416	0.766	0
9	O	0.422	0.619	0
10	O	0.419	0.406	0

Σ_a/Σ_t(.01: .04: .01) Iteration Number

Layer	Orig	20	1000	5000
		Image Density		
1	O	0	0	1.44E-4
2	O	0	0	0
3	O	0.023	0	0
4	X	0.360	0.170	0.120
5	X	0.719	1.17	1.37
6	X	0.938	1.86	1.99
7	X	1.05	1.95	0.709
8	O	1.09	1.54	0
9	O	1.09	0.925	0
10	O	1.08	0.149	0

Σ_a/Σ_t(.01: .06: .01) Iteration Number

Layer	Orig	20	1000	5000
		Image Density		
1	O	0	0	2.12E-4
2	O	0	0	0
3	O	0.042	0	0
4	X	0.556	0.302	0.211
5	X	1.09	1.78	2.17
6	X	1.40	2.66	2.79
7	X	1.55	2.55	0.209
8	O	1.59	1.65	0
9	O	1.58	0.453	0
10	O	1.54	0	0

Σ_a/Σ_t(.01: .08: .01) Iteration Number

Layer	Orig	20	1000	5000
		Image Density		
1	O	0	0	2.66E-4
2	O	0	0	0
3	O	0.062	0	0
4	X	0.724	0.441	0.313
5	X	1.40	2.30	2.87
6	X	1.77	3.21	3.14
7	X	1.94	2.77	0
8	O	1.96	1.29	0
9	O	1.93	0	0
10	O	1.87	0	0

Legend to Table 2: Values of reconstructed image densities of three-layer media. Media were infinitely long and wide, 10 MFP thick, and scattered photons isotropically. They were heterogeneous in only the depth dimension, the superficial layer boundary fixed at z = 3, the deep boundary fixed at z = 7, and the ratio Σ_a/Σ_t in the three layers variable from .01:.02:.01 to .01:.08:.01. Source and detector configurations, time windows, and number of unknowns all were the same as in Table 1.

deeper region was also correctly identified. At higher contrast, the calculated image density increased as would be expected, but showed signs of instability for media in which the absorption in the intermediate layer exceeded the background by ≥7%. This finding is not surprising, in view of the assumption of linearity for the perturbation equation. In effect, this assumption implies that an absorbing region does not cast a shadow.

It was further desirable to evaluate the perturbation model using experimental data. Time-resolved backscattered measurements were acquired as described in Methods by directing 100-fs pulses of light at 620 nm to a vessel containing diluted whole milk in which a 1-cm-diameter black aluminum sphere was positioned 5 mm below the surface. The transport MFP of the medium, as determined by transmission measurements[18], was 0.82 mm, while the absorption length was 253 mm. A raster-type scan was performed, involving 9 source locations. At each one, the backscattered flux was measured at five points along a straight line, between 2.5 and 12.5 mm from the source at 2.5 mm intervals. Thus, a total of 45 separate measurements were made. After accounting for symmetry, this number increased to 300 which served as the primary data for the reconstruction problem (i.e., although the absorber has infinitely many axes of symmetry, only three were used in the reconstruction). The location of these relative to the position of the target are shown in Figure 6 Panel A. Representative plots of normalized temporal profiles, $(\Delta I/I_0)$ vs. t, from which data were sampled are shown in Figure 6 Panel B. For a given profile, a total of 3 time intervals were selected; one just prior to departure of the ordinate value from zero, one in the middle of the rising phase and one in the plateau region. The time intervals over which these values were sampled are indicated by the dotted lines.

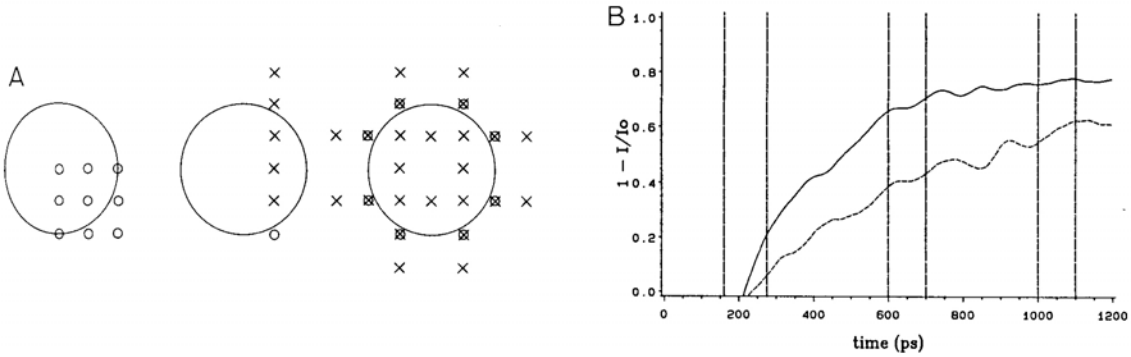

Legend for Figure 6: Panel A: Locations of source and detector fibers relative to spherical absorber in the experimental setup. Left, the nine relative positions of the source fiber (small circle); reconstruction program allowed symmetry of absorber (large circle) to increase the number to twenty five. Middle, the five positions of the detector fiber (cross) relative to the source, for a single source fiber location. Right, reconstruction program allowed symmetry of absorber to increase the number of source and detector fibers from one and five to eight and forty, respectively. Panel B: Reduction of intensity of measured backscattered light, relative to absorberless reference medium, vs. time. Data were smoothed by calculating at 31-point moving average prior to graphing. For both curves shown, the fibers are separated by 12.5 mm; in both cases the source fiber is placed over an edge of the absorber. The top (solid) curve is the result when the source-detector line bisects the absorber; the bottom (dashed) curve is the result when the absorber lines on one side of the source-detector line. The three pairs of dashed vertical lines show the time intervals from which the three data points used in the reconstruction were selected for all measurements made at r = 12.5 mm.

In an effort to reduce computation time and the complexity of the algorithm, simplifications were introduced. The first involved a rescaling of the problem to a more coarse grid. Data corresponding to a given time interval were assigned to time-resolved weight functions calculated for a half-space medium with isotropic scattering and $\Sigma_a = .01\Sigma_t$, with detectors oriented normally to the medium and positioned between 1 and 5 MFP from the source in steps of 1 MFP. The time intervals over which the weight functions were calculated were 0-4, 4-8, 8-12 MFT for each detector location. In this manner, the weight functions for detectors r = 1, r = 2,..., r = 5, for each time interval, were assigned to detectors positioned 2.5, 5, ..., 12.5 mm from a source. Thus a total of 15 different time-resolved weight functions were used in the reconstruction calculation.

The second simplification was the use of a given weight function to cover a range of time points in the temporal profiles. Overall, both approximations introduce an averaging effect which will serve to reduce the recoverable resolution. In addition, the problem was underdetermined, as the amount of input data was only 15% of the number of unknowns. The resultant calculated image, using a scheme progressive in position and time, is shown in Figure 7. Inspection reveals that whereas the image obtained is very crude, evidence for a structure having a curved surface located below the surface of the medium is present.

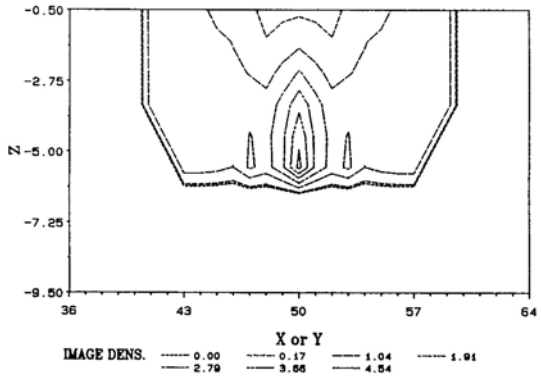

Legend to Figure 7: Contour plot of vertical section through image of spherical absorber, reconstructed by equations 6a and 6b, and using time-resolved weight functions and experimental reflectance measurements. Data from three hundred source detector pairs (see Figure 6A) and three time windows (see Figure 6B) were used in the reconstruction. Weight functions employed were those for a half-space medium with $\Sigma_a = .01\Sigma_t$, with the weight functions for r = 1,2,3,4, and 5 MFP assigned to the detector fibers placed, respectively, 2.5, 5.0, 7.5, 10.0, and 12.5 mm from the source. The time windows 0-4, 4-8, and 8-12 MFT were assigned to the three data points chosen for the reconstruction from each of the temporal profiles.

4.0 Discussion

The current report extends our studies on the backscattering imaging problem in dense scattering media to include use of time-resolved signals. While no attempt was made to preform a systematic survey, evidence obtained does indicate the following. Evaluation of the linear perturbation equation with time-resolved signals permits the recovery of images having higher resolution than is achieved with steady-state signals. At this point it is not clear whether this represents a fundamental property of the measurement schemes or is more of a function of the computational effort employed to evaluate the problems.

While a less rigorous approach was used here to evaluate the perturbation equation than described by Wang et al.[17], the observation that portions of the reconstructed image contained evidence of high resolution is very encouraging. This optimistic interpretation is further supported when it is noted that, in all cases, the images obtained were based on underdetermined problems in which the view angle of measurement was severely restricted (i.e., only backscattered measurements were performed). Results of evaluation of the three-layer problem also support an optimistic perspective. The calculated images showed that, in many cases, both the top and bottom boundaries were well-resolved, even in the case of only 1% absorption contrast between layers.

A heuristic strategy introduced in the evaluation of the perturbation equation is the idea of evaluating the data in a progressive manner. This scheme appears analogous to a layer-stripping approach and makes use of the *a priori* knowledge that whatever the interior gradient of detected photons is, it will always be steepest for detectors located closest to the source, and decline for more distant detectors. When extended to the time domain, a scheme progressive in time can also be considered. The limited evidence obtained suggest that this may also be helpful.

Another heuristic strategy we have recently begun to consider has been to express the value of a weighting function in a given voxel as the fraction of the total weight for a particular source-detector pair instead of its absolute value. The idea here is that whereas the absolute value of the weight in a given voxel will always decrease with increasing distance separating source and detector, the fraction of the total weight for the voxel when compared to other source-detector configurations need not vary monotonically. The reason for this is that the weight gradient varies with the source-detector configuration and as a function of time. Thus the fractional value of the weight for a source-detector pair in a voxel may be several times greater than for the same voxel but different source-detector pair, even though its absolute value is less. The significance of this is that it potentially allows for a differential weighting of the weight functions in a manner which serves to improve discrimination of the contribution of the signals from greater depths from those originating predominately from more shallow depths.

As is the case for the results presented by Wang et al[17], data shown here constitute only one step of the perturbation equation. An iterative solution would require that output from the inverse solution be used as input for the forward problem.

Evaluation of the latter will require the use of numerical methods such as Monte Carlo methods or a relaxation solver described by Schlereth et al.[1,2], among others. While hard evidence is lacking, we believe that an iterative solution of the perturbation equation in a progressive manner might well prove a more effective approach to image recovery, particularly for the case in which signals about the target are evaluated. The idea here is that before any reasonable assessment of the optical properties of the interior of a diffusing media is possible, good assessment of the more superficial layers must first be made. This assertion is based partly on a practical consideration of the size of the computation required for a problem in which all detector readings are evaluated simultaneously. A schematic of this approach is depicted in Figure 8. Image recovery would proceed by considering first the family of detectors that lie closest to a source, for all source positions. Iterative solution of the forward and inverse problems would result in a scoring of voxels which lie near the surface. Consideration of more distant detectors (and/or at later times) would lead to determination of deeper layers.

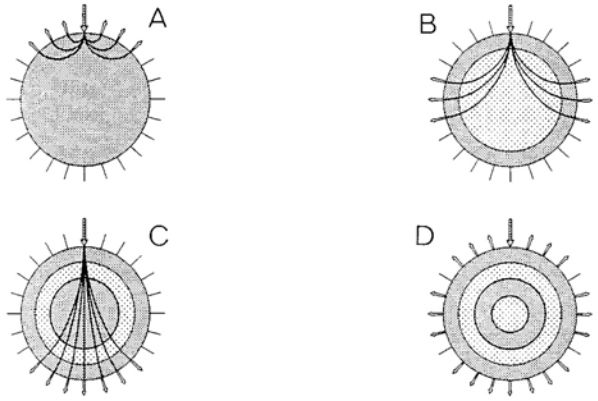

Legend to Figure 8: Proposed "layer-stripping" approach for improved resolution of interior regions of a highly scattering medium. Method considers a progressive iterative analysis of the inverse and forward problem. Data yielding the most reliable information about near surface structures are first considered (A). This information is used to update the forward problem which is then used to evaluate detector values which preferentially probe to successively greater depths (B). Transmission measurements serve to best define properties of the most interior regions (C), yielding the final image (D).

The approach described here is one of several our group is evaluating for the image recovery problem. A satisfactory solution will require the consideration of several factors: use of *a priori* data to constrain permissible values[15,19], appropriate modeling of the forward problem to account for refraction and reflection of photons across internal boundaries[20], iterative updates of the forward problem[1,2], efficient error-minimization protocols[17], and consideration of a suitable computing platform[1,2], among others. Although our emphasis has been on examining backscattered signals, this has been based largely on consideration of practical constraints likely encountered in any acute care setting. It seems likely that measurements about an object will prove best. Recent reports by Arridge et al.[16], Singer et al.[21] and Grünbaum et al.[22] support this view. While much more development is required to optimize the imaging algorithms, results reported here indicate that fairly high resolution images can be obtained for simple structures, using only backscattered signals, to a depth of at least 7 transport MFP.

5.0 References

1. F. H. Schlereth, J. M. Fossaceca, A. D. Keckler and R. L. Barbour, "Multicomputer based neural networks for imaging in random media", in *IEEE Proc. Nuclear Science Symposium*, Nov. 1991, In Press.

2. F. H. Schlereth, J. M. Fossaceca, A. D. Keckler and R. L. Barbour, "Imaging in diffusing media with a neural net formulation: A problem in large scale computation". SPIE, vol 1641, accompanying paper in these proceedings, 1992.

3. R. Aronson, R. L. Barbour, J. Lubowsky and H. Graber, "Application of Transport Theory to NIR Medical Imaging," in *Modern Mathematical Models in Transport Theory; Advances and Applications*, Vol. 51, pp 64-75, Birkhauser Press, 1991.

4. R. L. Barbour, H. L. Graber, R. Aronson and J. Lubowsky, "Imaging of subsurface regions in random media by remote sensing", in *Proc. Time-Resolved Spectroscopy and Imaging of Tissues*, SPIE Vol. 1431, pp 192-203, 1991.

5. R. L. Barbour, H. Graber, R. Aronson and J. Lubowsky, "Model for 3-D Optical Imaging of Tissue", in 10th *Annual International Geoscience and Remote Sensing Symposium* (IGARSS), Vol. II, pp. 1395-1399, 1990.

6. R. L. Barbour, H. Graber, J. Lubowsky and R. Aronson, "Monte Carlo Modeling of Photon Transport in Tissue. V. Model for 3-D Optical Imaging of Tissue", Biophys. J., 57, p. 382a, abst. no. 603, 1990.

7. J. G. Webster, ed., *Electrical Impedance Tomography*. Adam Hilger, Bristol, England,1990.

8. B. Chance, et al. "Comparison of time-resolved and unresolved measurements of deoxyhemoglobin in brain", in Proc. Nat. Acad. Sci. vol. 85, 4971-4975, 1988.

9. K. M. Yoo, Q. Xing, and R. R. Alfano, "Imaging object hidden in highly scattering media using femtosecond second harmonic generation cross-correlation time-gating", Opt. Lett., 16, 1019, 1991.

10. R. R. Alfano, P. P. Ho, and K. M. Yoo, "Photons for prompt tumor detection", Physics World, 5, 37, 1991.

11. L. M. Wang, P. P. Ho, C. Liu, G. Zhang and R. R. Alfano, "Ballistic 2-D imaging through scattering walls using an ultrafast optical Kerr gate", Science, 253, 769, 1991.

12. G. Hebden and R. A. Kruger, "A time-of-flight breast imaging system: spatial resolution performance," in *Proc. Time Resolved Spectroscopy and Imaging of Tissues*", SPIE Vol. 1431, pp 225-231, 1991.

13. J. Fishkin, E. Gratton, M. J. vandeVen and W. W. Mantulin, "Diffusion of Intensity Modulated Near-Infrared Light in Turbid Media", ibid, pp 122-135, 1991.

14. E. M. Sevick, B. Chance, J. Leigh, S. Nioka and M. Maris, "Quantitation of Time- and Frequency-Resolved Optical Spectra for the Determination of Tissue Oxygenation", Anal. Biochem., 195, 330-351, 1991.

15. H. L. Graber, R. L. Barbour, J. Lubowsky, R. Aronson, B. B. Das, K. M. Yoo and R. R. Alfano, "Evaluation of Steady-State, Time- and Frequency-Domain Data for the Problem of Optical Diffusion Tomography", SPIE Vol. 1641, accompanying paper in these proceedings, 1992.

16. S. R. Arridge, P. van der Zee, M. Cope, and D. T. Delpy, "Reconstruction methods for infra-red absorption imaging", in *Proc.Time Resolved Spectroscopy and Imaging of Tissues*", SPIE Vol. 1431, pp 204-215, 1991.

17. Y. Wang, J. H. Chang, R. Aronson, R. L. Barbour, H. L. Graber and J. Lubowsky, "Imaging of Scattering Media by Diffusion Tomography: An Iterative Perturbation Approach", SPIE Vol. 1641, accompanying paper in these proceedings, 1992.

18. K. M. Yoo, F. Liu, R. R. Alfano, "When Does the Diffusion Approximation Fail to Describe Photon Transport in Random Media?", Phys. Rev. Lett., 64, pp 2647-2650, 1990. Erratum: op. cit., 65, p 2210, 1990.

19. R. L. Barbour, H. L. Graber, R. Aronson and J. Lubowsky, "Determination of Macroscopic Optical Properties of Multilayer Random Media by Remote Sensing", in *Proc. Time Resolved Spectroscopy and Imaging of Tissues*", SPIE Vol. 1431, pp 52-62, 1991.

20. R. Aronson, "Exact Interface Conditions for Photon Diffusion", SPIE Vol. 1641, accompanying paper in these proceedings, 1992.

21. J. R. Singer, F. A. Grünbaum, P. Kohn and J. P. Zubelli, "Image reconstruction of the interior of bodies that diffuse radiation", Science, vol. 248, pp. 990-993, 1990.

22. F. A. Grünbaum, P. Kohn, G. A. Latham, J. R. Singer and J. P. Zubelli, "Diffuse tomography", in *Proc. Time-Resolved Spectroscopy and Imaging of Tissues*, SPIE Vol. 1431, pp 232-238, 1991.